51st AIAA Aerospace Sciences Meeting including the New Horizons Forum and Aerospace Exposition
07 - 10 January 2013, Grapevine (Dallas/Ft. Worth Region), Texas

AIAA 2013-0608

Accuracy of State-of-the-Art Actuator-Line Modeling for Wind Turbine Wakes

Pankaj K. Jha[1]
The Pennsylvania State University, University Park, PA, 16802

Matthew J. Churchfield[2] and Patrick J. Moriarty[3]
National Renewable Energy Laboratory, CO, 80401

Sven Schmitz[4]
The Pennsylvania State University, University Park, PA, 16802

The current actuator line method (ALM) within an OpenFOAM computational fluid dynamics (CFD) solver was used to perform simulations of the NREL Phase VI rotor under rotating and parked conditions, two fixed-wing designs both with an elliptic spanwise loading, and the NREL 5-MW turbine. The objective of this work is to assess and improve the accuracy of the state-of-the-art ALM in predicting rotor blade loads, particularly by focusing on the method used to project the actuator forces onto the flow field as body forces. Results obtained for sectional normal and tangential force coefficients were compared to available experimental data and to the in-house performance code XTurb-PSU. It was observed that the ALM results agree well with measured data and results obtained from XTurb-PSU except in the root and tip regions if a three-dimensional Gaussian of width, ε, constant along the blade span is used to project the actuator force onto the flow field. A new method is proposed where the Gaussian width, ε, varies along the blade span following an elliptic distribution. A general criterion is derived that applies to any planform shape. It is found that the new criterion for ε leads to improved prediction of blade tip loads for a variety of blade planforms and rotor conditions considered.

Nomenclature

ABL	=	Atmospheric boundary layer
ADM	=	Actuator disk method
ALM	=	Actuator line method
AOA	=	Angle of attack [deg]
AR	=	Blade aspect ratio
BEM	=	Blade element momentum
c	=	Airfoil chord [m]
CFD	=	Computational fluid dynamics
C_n	=	Sectional normal force coefficient
C_t	=	Sectional tangential force coefficient
C_P	=	Coefficient of power
C_T	=	Coefficient of thrust
HVM	=	Helicoidal vortex method
LES	=	Large-eddy simulation
NREL	=	National Renewable Energy Laboratory
RANS	=	Reynolds-Averaged Navier-Stokes

[1] Graduate Research Assistant, Department of Aerospace Engineering, AIAA Student Member
[2] Research Engineer, National Wind Technology Center, AIAA Member
[3] Senior Engineer, National Wind Technology Center, AIAA Member
[4] Assistant Professor, Department of Aerospace Engineering, AIAA Member

RPM = Revolutions per minute [1/min]
V_{wind} = Mean wind speed

I. Introduction

Wind energy is currently one of the most readily available sources of renewable energy. Various reports[1-3] state that high penetrations of wind-driven electrical generation, 20% and greater of the electrical demand, are technically feasible. However, the wind industry faces a number of challenges today in developing wind farms both on shore and off shore, some of which involve the aerodynamics within the wind farm. Wind turbine wakes interact with turbines located downstream, with other wakes, and with the turbulent atmospheric boundary layer (ABL). The aerodynamic interaction between multiple wind turbines in an array is a function of the coefficient of thrust, C_T, the separation distance between rotors, the yaw angle to the incident wind, and the physics of the driving ABL flow with varying atmospheric stability states. Although accurate wake modeling is necessary to predict mean power production, the bigger challenge is to understand the details of how wakes affect transient mechanical loading and power production. It is here that the actuator turbine aerodynamics concept, in conjunction with CFD, offers the potential for accurately predicting unsteady wind turbine wakes at a feasible computational cost. This places actuator methods between low-fidelity engineering models[4-8] and fully blade-resolved CFD simulations. The reduced cost of actuator simulations as opposed to fully blade-resolved simulations enables the simulation of an entire wind plant consisting of hundreds of turbines and subject to resolved turbulent inflow using large-eddy simulation (LES). At this time, fully blade-resolved simulations subject to resolved turbulent inflow are only possible with hybrid Reynolds-averaged Navier-Stokes (RANS)-LES, which is computationally expensive and precludes the simulation of an entire wind plant.

The lowest-order actuator-type method to model wind turbines is the actuator disk method (ADM) that was first developed for RANS solvers by Sørensen[9], Leclerc and Masson[10-11], Réthoré et al.[12], and Mikkelsen[13]. The actuator disk concept allows replacing the actual wind turbine rotor by a disk of rotor-azimuth-averaged body-force that enters the momentum equations of the underlying flow solver. Details, such as the blade root and tip vortices, are not accounted for because the rotor is modeled as a disk. However, unsteady interaction of the overall wake with the turbulent ABL flow is accounted for. At present, a fair number of efforts are underway that use large-eddy simulations and the actuator disk concept to model large wind farms. Some examples are the works of Ivanell et al.,[15] Meyers and Meneveau,[16] Singer et al.,[17] and Stovall et al.[19]

The actuator line method (ALM) represents each rotating blade as a line of force rotating through the flow field. Details such as root and tip vortices are captured, and, hence, the ALM is the next level of increased fidelity relative to the ADM. Most of the current state-of-the-art ALMs are rooted in the work of Sørensen and Shen[20] in a RANS solver. Further developments followed by Troldborg et al.[21-23] and Sibuet Watters and Masson.[24] Some examples of the use of the ALM in conjunction with LES are the works of Lu and Porté-Agel,[14] and Conzemius et al.[18] Recently, the ALM of Sørensen and Shen[20] has been implemented into an ABL-LES solver created with OpenFOAM[27] by researchers at the National Renewable Energy Laboratory (NREL).[28-31] The solver has demonstrated its potential to model large wind farms and overall wake effects. Actuator line methods model time-varying turbine loads by a suitable distribution of body forces along the blade whose strengths are determined from sectional inflow conditions and blade-element type table lookup of airfoil properties. In order to prevent numerical instabilities, and to transform the line force into a volumetric force, the body-forces are projected over a finite distance around the actuator line. Most commonly, the projection function has a Gaussian shape.[9,13,20,21-23] In the past few years, the ALM concept has been extended to actuator surface methods, some examples are the works of Dobrev et al.,[25] Shen et al.,[26] and Sibuet Watters and Masson,[24] yet thus far with no apparent advancement in modeling accuracy.

This work aims at quantifying and improving the capability of state-of-the-art ALM modeling in predicting spanwise blade loads along with rotor thrust and power. Though the ALM has advanced to become one of the most widely accepted computational methods for predicting the wakes of individual wind turbines and wake interactions in turbine arrays and larger wind farms, there is a need within the wind energy community for guidelines in choosing a suitable set of ALM parameters, for example grid spacing and stretching, the number of actuator points along the blade, the Gaussian radius required for the body-force projection etc., that lead to consistent results among various rotor designs. The wind energy community is now well aware of the fact that the atmospheric stability state plays an integral role in the recovery of the wake momentum deficit downstream of a wind turbine, thus having a profound effect on the performance of a given wind turbine array or wind farm.[31,39] In principle, the ALM is suitable to model these effects as the required grid spacing is of the order of the blade chord and can resolve turbulent eddies up to that scale and their interaction with turbulent eddies that were generated and advected by the ABL flow. However, a rigorous study is missing that quantifies how well state-of-the-art ALM predicts sectional blade loads

that define all these interactions. This is largely due to the fact that blade loads data other than rotor thrust and power are difficult to attain and analyze from field measurement campaigns. In this work, the authors perform a rigorous study on assessing ALM accuracy through comparison against available data, classical lifting-line solutions, and a blade-element momentum (BEM) method. All simulations are conducted with steady and uniform inflow only.

The paper is organized as follows: Section II gives a brief description of the ALM and its implementation in OpenFOAM. Furthermore, a method for a variable Gaussian spreading width along the blade span is presented that is based on the recent work of Shives and Crawford.[40] Then, a more general method of a variable spreading width is proposed where the Gaussian spreading width is based on an equivalent elliptic blade planform of the same aspect ratio (AR) than the original blade. A brief introduction is given to the performance code XTurb-PSU, which is based on BEM and used for comparing blade loads for some of the test cases described below. Section III begins with a description of the grids used in the simulations. The NREL Phase VI rotor is used as a first test case to demonstrate current shortcomings of the ALM in predicting the blade tip loads. The paper then turns its attention to non-rotating (or parked) conditions and presents results obtained for the NREL Phase VI rotor and wing cases with an elliptic lift distribution. Various values for the Gaussian spreading width are considered, and the results obtained are discussed. In particular, a variable Gaussian spreading width based on an equivalent elliptic blade planform is found to give consistent results between various blade designs considered. The adjusted spreading methods are applied to rotating conditions for the NREL Phase VI rotor and the NREL 5-MW turbine, the latter one being compared to results obtained from the XTurb-PSU code only. The paper concludes with some recommendations for users of the ALM and provides an outlook to future research.

II. Numerical Methods

A. Actuator-Line Method (ALM) in OpenFOAM

The OpenFOAM (Open Field Operations and Manipulations) CFD toolbox[27] is a set of C++ libraries meant for solving partial differential equations. The governing equations are solved using the finite-volume method on unstructured meshes. All variables are cell-centered and collocated on the grid. To avoid the pressure-velocity decoupling that occurs with collocated, incompressible solvers, the velocity fluxes at the finite-volume faces are constructed using an interpolation similar to that of Rhie and Chow.[41] All other interpolation from cell centers to faces is a mix of predominantly either linear (second-order central differencing) or midpoint (second-order central differencing with equal weighting regardless of mesh stretching) with a small amount of first-order upwinding. The reason for this will be discussed below. Time advancement uses Issa's[42] PISO (Pressure-Implicit Splitting Operation) algorithm, which is an implicit predictor/corrector scheme. The implicit terms are integrated in time using second-order Crank-Nicolson discretization. We use one predictor followed by three correctors. The momentum transport equation is solved directly. However, to enforce the continuity equation, the divergence of the discrete momentum transport equation is taken, which results in an elliptic equation for the modified pressure. The momentum transport equations are solved using an iterative diagonal incomplete-LU pre-conditioned biconjugate-gradient linear system solver. The pressure equation, which is the most expensive to solve, is solved using a geometric agglomerated algebraic multigrid solver. The code is parallelized using the message-passing interface (MPI).

As discussed above, the spatial interpolation used in this study is a blend of linear/midpoint and upwind interpolation. As the flow encounters the actuator line body-force field, some oscillations are observed in velocity and pressure emanating from the actuator line if pure linear or midpoint interpolation is used, which is shown in Fig. 1(a). Even using Troldborg's rule of thumb in which $\boldsymbol{\varepsilon/\Delta r = 2}$, these oscillations occur. Troldborg, however, used a blend of 90% fourth-order central differencing and 10% third-order QUICK upwind differencing. To remove these oscillations, we tried using a blend of 90% second-order linear / 10% first-order upwind interpolation upstream of the actuator line and 98% linear / 2% upwind everywhere else with a smooth transition in blending between these zones. This was successful in removing the oscillations without producing excessive artificial diffusion in the region of interest around the actuator lines and in their wakes. However, when we used a stretched grid (only for the fixed wing cases), an "imprint" of the grid stretching appeared in the flow field upstream of the actuator. (The imprint can be observed in Fig. 1(a) as the deep red and blue regions ahead of the actuator point.) Wesseling[43] explains that midpoint interpolation in which the cell face value is the simple average of the two surrounding cell center values regardless of grid stretching (which is identical to linear interpolation on a uniform grid) can often be more accurate than the weighted interpolation of the second-order linear interpolation scheme, which is sensitive to

grid stretching. In short, Wesseling says that linear interpolation "is more prone to wiggles" than midpoint interpolation. Therefore, in order to successfully eliminate oscillations caused by the actuator line and the "imprint" of the stretched mesh, we used a blend of 90% midpoint / 10% upwind upstream of the actuator and 98% midpoint / 2% upwind everywhere else with a smooth transition in the blending between these two regions. The oscillation and

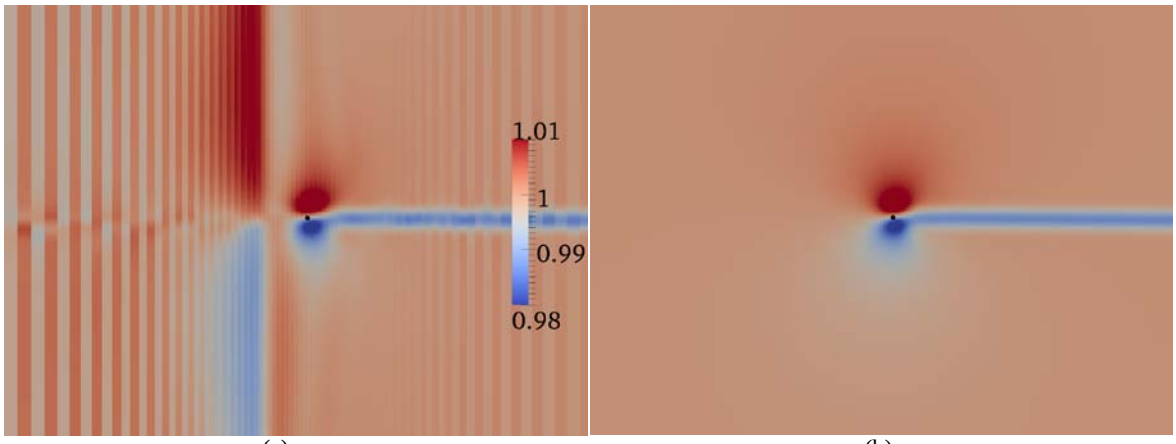

(a) (b)

Figure 1. A contour of the streamwise velocity normalized by freestream velocity taken in a plane perpendicular to the actuator line and at midspan for the fixed wing stretched grid case using purely linear interpolation (a) or a spatially varying blend of midpoint and upwind interpolation (b). The point where the actuator line intersects these contours is shown with a black dot.

imprint free solution are shown in Fig. 1(b).

The ALM within OpenFOAM is being actively developed and maintained by researchers at NREL.[28-31] As mentioned in section I, the ALM is that of Sørensen and Shen[20], and the underlying LES solver is capable of modeling both uniform and ABL flow.[28-31] The ALM finds sectional lift and drag forces by determining the local flow velocity and angle of attack (AOA) that is then applied to an airfoil lookup table. In this work, local velocity is sampled directly at the center of each actuator line element, and the angle of attack is taken to be equal to the local flow angle. Since the velocity is sampled at the center of each actuator element, which is the center of the bound vortex circulating about the actuator line, the effects of the upwash and downwash created by the bound vortex are not seen. The blade is discretized into a finite number of (typically 25-40) actuator points. The lift and drag forces computed at these actuator points are projected onto the background Cartesian grid as body forces in the momentum equation. The last term in the momentum equation (1) corresponds to the body-force term.

$$\frac{D\boldsymbol{u}}{Dt} = \text{RHS} + \mathbf{F}_p \tag{1}$$

The body-force term indirectly imposes a pressure jump across the actuator line. The projection of the body forces that represent the blade loads is typically achieved by a Gaussian function as shown in equation (2).

$$\mathbf{F}_p(x_p, y_p, z_p, t) = -\sum_N \sum_m \mathbf{f}_{N,m}(x_{N,m}, y_{N,m}, z_{N,m}, t\,)\,\eta_{N,m} \tag{2}$$

where $$\eta_{N,m} = \frac{1}{\varepsilon^3 \pi^{3/2}} exp\left[-\left(\frac{|\boldsymbol{r}|}{\varepsilon}\right)^2\right] \tag{3}$$

Here N is the blade index, m is the actuator point index, and $|\boldsymbol{r}|$ is the distance from grid cell p to the actuator point. A more detailed description of the solver has been presented in an earlier work.[28-31]

A.1 Grid-Based Gaussian Spreading Width[22,33], $\boldsymbol{\varepsilon/\Delta r}$ = constant

A common rule-of-thumb states that $\boldsymbol{\varepsilon}$ should be chosen as small as possible, however a minimum threshold exists in order to avoid numerical instabilities that occur when the radius of the body force applied to Eqn. (1) is too small such that it resembles a discontinuity. These instabilities appear as "ringing" when the convection term of the momentum equation is discretized using central differencing. Troldborg,[22] therefore, suggests a Gaussian spreading width (or radius) $\boldsymbol{\varepsilon/\Delta r = 2}$ of twice the radial grid spacing $\boldsymbol{\Delta r}$ in order to maintain numerical stability and to obtain

good predictions of the rotor power to within a few percent. A detailed study of the effect of the Gaussian width $\boldsymbol{\varepsilon}$ in conjunction with grid resolution has been performed by Martínez et al.[33] They found that at a given inflow wind speed and a given $\boldsymbol{\varepsilon}$, the computed rotor power converges as the grid is refined; however, as $\boldsymbol{\varepsilon/\Delta r}$ is varied from 2 to 10.5, the predicted power increases by about 25%, which is significant.

A.2 Chord-Based Gaussian Spreading Width[40], ε/c = constant

It has only been recently shown that sectional blade inflow conditions have been considered in the context of ALM accuracy in addition to computed rotor thrust and/or power. It is the local induced flow at a section of blade that defines a blade section's angle of attack (AOA) and hence local lift and drag forces. Shives and Crawford[40] performed simulations of an elliptic wing of $AR = 10.2$ and investigated how the Gaussian spreading width $\boldsymbol{\varepsilon}$ affects the computed inflow, in particular the downwash, at the actuator line. They found that it is advantageous to choose $\boldsymbol{\varepsilon}$ based on the local blade chord $\boldsymbol{c}$. It was found that $\boldsymbol{\varepsilon/c}$ **= 0.25** is suitable to compute the expected constant downwash distribution at an elliptically loaded lifting (or actuator) line at a high accuracy given that $\boldsymbol{\varepsilon \geq 4\Delta r}$.

Though their work is very promising and suggests that the Gaussian spreading width $\boldsymbol{\varepsilon}$ should be chosen relative to the actual blade planform, i.e. the blade chord $\boldsymbol{c}$, one can argue that the proposed method breaks down for a rectangular wing that is twisted such that an elliptic lift distribution with constant downwash is achieved. In this case, the $\boldsymbol{\varepsilon/c}$ = constant criterion results in a constant Gaussian spreading width $\boldsymbol{\varepsilon}$ along the blade span, and the actual grid spacing $\boldsymbol{\Delta r}$ determines what the value for $\boldsymbol{\varepsilon/\Delta r}$ will be.

A.3 Elliptic Gaussian Spreading Width, $\varepsilon/c*$ = constant

In the following section, a new method for determining the Gaussian spreading width $\boldsymbol{\varepsilon}$ is proposed that takes into account the lessons learned from the spreading methods described in sections A.1 and A.2. It appears that the Gaussian spreading width $\boldsymbol{\varepsilon}$ should be as small as possible in order to resemble accurately an actuator line while maintaining numerical stability. In addition, a blade-conforming $\boldsymbol{\varepsilon}$ along the span has shown to improve the blade-inflow distribution along an elliptically loaded wing and has resulted in an improved prediction of the downwash at the actuator line as well as of the blade tip loads.[40]

In the special case of a wing with an elliptic planform, the chord distribution resembles the actual spanwise blade loading. It can be hence hypothesized that the Gaussian spreading width $\boldsymbol{\varepsilon}$ should be proportional to the actual magnitude of the sectional blade force rather than the blade planform. This intrinsically avoids spreading beyond the blade tips as loads tend to zero there. Unfortunately, the blade load distribution is part of the actual solution and therefore unknown a priori. Furthermore, one wants to avoid a time-dependent spreading width $\boldsymbol{\varepsilon}$ at a given blade section as the solution evolves. This is likely to cause numerical instabilities in a time-dependent flow and would probably require costly sub-iterations of the solver.

Nevertheless, we move forward the idea of an elliptic distribution being a first-order representation of a general blade loading. Indeed, the elliptic loading is the first mode of a general Fourier-series solution for the blade loading. Next, we develop a variable spreading width $\boldsymbol{\varepsilon}$ by following these steps:

1. Determine the blade aspect ratio, $\boldsymbol{AR}$

$$\boldsymbol{AR} = \frac{\boldsymbol{R}}{\bar{\boldsymbol{c}}} \quad ; \quad \bar{\boldsymbol{c}} = \frac{\boldsymbol{1}}{\boldsymbol{R}}\int_{\boldsymbol{0}}^{\boldsymbol{R}} \boldsymbol{c}(\boldsymbol{r})\boldsymbol{dr} \tag{4}$$

   where $\boldsymbol{R}$ is the wing span or blade radius and $\bar{\boldsymbol{c}}$ is the average blade chord.

2. Find a 'fictitious' elliptic planform with the same $\boldsymbol{AR}$.

$$\boldsymbol{c}^*(\boldsymbol{r}) = \boldsymbol{c_0}\sqrt{\boldsymbol{1} - \left(\frac{\boldsymbol{2r}}{\boldsymbol{R}}\right)^{\boldsymbol{2}}} \quad ; \quad \boldsymbol{c_0} = \frac{\boldsymbol{4}}{\boldsymbol{\pi}}\bar{\boldsymbol{c}} \tag{5}$$

3. Postulate the following:
   a. $\boldsymbol{\varepsilon(r)/c^*(r) = \varepsilon_0/c_0 = const.}$ (6)
   b. $\boldsymbol{\varepsilon_0 = n_{max}\Delta r}$ (7)
   c. $\boldsymbol{\varepsilon_{R/2} = n_{min}\Delta r}$ (8)

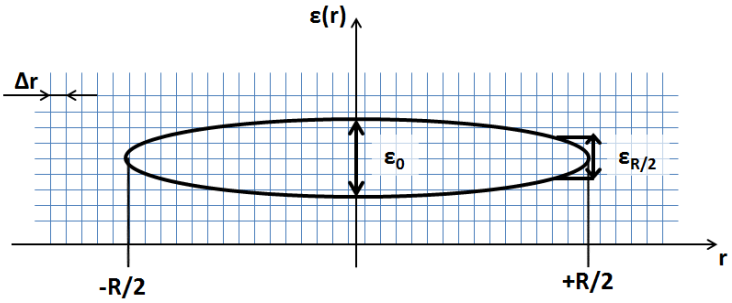

Figure 2. Elliptic distribution of Gaussian spreading width, ε.

Here $\boldsymbol{n_{min}}$ and $\boldsymbol{n_{max}}$ are dimensionless factors that define minimum and maximum spreading width $\boldsymbol{\varepsilon}$ for a given grid spacing $\boldsymbol{\Delta r}$. Equations (5), (7), and (8) in (6) yield

$$\boldsymbol{\varepsilon(r) = MAX}\left(\boldsymbol{n_{max}\,\Delta r}\sqrt{\mathbf{1}-\left(\frac{2r}{R}\right)^2}\;;\; \boldsymbol{n_{min}\Delta r}\right), \tag{9a}$$

which describes an elliptic distribution of the Gaussian spreading width $\boldsymbol{\varepsilon}$ with user-specified minimum and maximum spacing (see Figure 2 for an illustration). Alternatively, Equations (4)-(8) can be combined to obtain a criterion for the Gaussian spreading width $\boldsymbol{\varepsilon}$ in relation to the 'ficticious' elliptic planform $\boldsymbol{c^*}$ in Equation (5), i.e.

$$\boldsymbol{\varepsilon/c^* = 0.25\, n_{max}\frac{\Delta r}{R}(\pi AR)} = \textbf{constant} \tag{9b}$$

In Equation (9b), a general width $\boldsymbol{\varepsilon/c^*}$ criterion becomes a function of a given grid resolution $\boldsymbol{\Delta r/R}$ along the actuator line, the blade aspect ratio $\boldsymbol{AR}$, and a single user-specified discretization parameter $\boldsymbol{n_{max}}$. It is interesting to note that the $\boldsymbol{\varepsilon/c^* = 0.25}$ criterion from Shives and Crawford[40] is recovered for an $\boldsymbol{AR}$ =10.2 elliptic planform and the grid resolution and minimum spreading width specified in their work.

Figure 3 shows the 'fictitious' elliptic planform areas $\boldsymbol{c^*}$ for the NREL Phase VI rotor and the NREL 5-MW turbine.

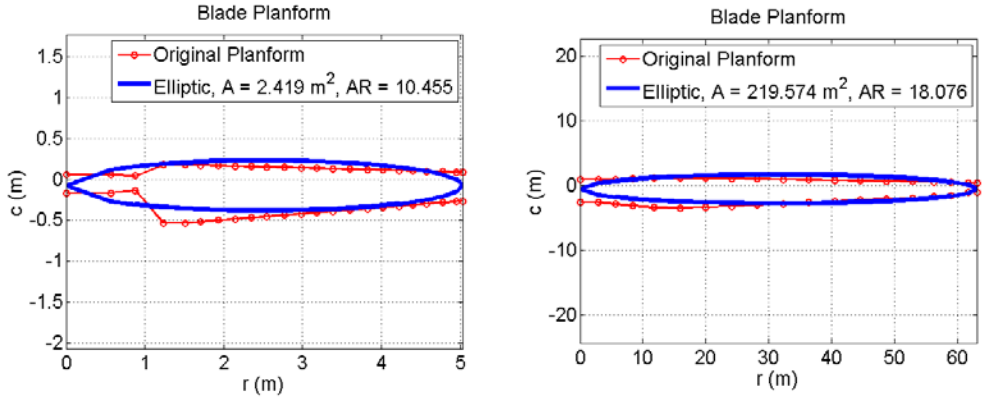

(a) NREL Phase VI rotor **(b) NREL 5-MW turbine**

Figure 3. Examples for the 'fictitious' elliptic planform.

B. XTurb-PSU

In addition to the CFD simulations described in part A above, an in-house developed wind turbine design and performance prediction code, XTurb-PSU,[32] was used for a comparative study. XTurb-PSU uses either Blade element momentum (BEM) theory based on NREL's AeroDyn code[34] or a prescribed Helicoidal vortex method (HVM).[35] It also employs a stall delay model by Du and Selig[36] rooted in NREL's AirfoilPrep worksheet.[37] The HVM module in XTurb-PSU is also capable of analyzing wind turbines under parked conditions and fixed wings in steady flow. This makes the XTurb-PSU code a flexible performance tool for both the rotating and parked test cases considered in this work.

III. Results and Discussion

ALM simulations were performed on two different types of grids. The first grid type has various refined zones within an outer baseline grid. Typically, 3 to 6 layers of refinement are used. An illustration is given in Figure 4(a). The outer grid dimensions span from -4D to 8D in the streamwise and -5D to +5D in the other two directions with the turbine location as the reference point. The innermost refinement region extends from -0.5D to 3D in the streamwise and -1D to +1D in the other two directions. All refinement regions contain uniform cell dimensions where the grid is refined by a factor of two in all directions in each successive refinement zone. The domain sizes used are similar to those documented in the literature.[22,33] The second type of grids used for fixed wing cases only, are refined near the wing tips and near the actuator line and stretch out towards the mid-span and away from the actuator line. Such a grid is illustrated in Figure 4(b). In general, the grid stretching follows a geometric progression with an expansion factor in the range 1.03 to 1.06 or is determined by a cosine distribution. The resolution near the blade tips is approximately 1% of the blade span or radius. The grid sizes used in this work are close to 5 million cells.

The time steps used in the simulations are determined by a more stringent condition than the standard CFL criterion. In all cases, the time step is chosen such that the blade tip does not traverse more than one grid cell in the innermost refined zone close to the actuator line in one time step.

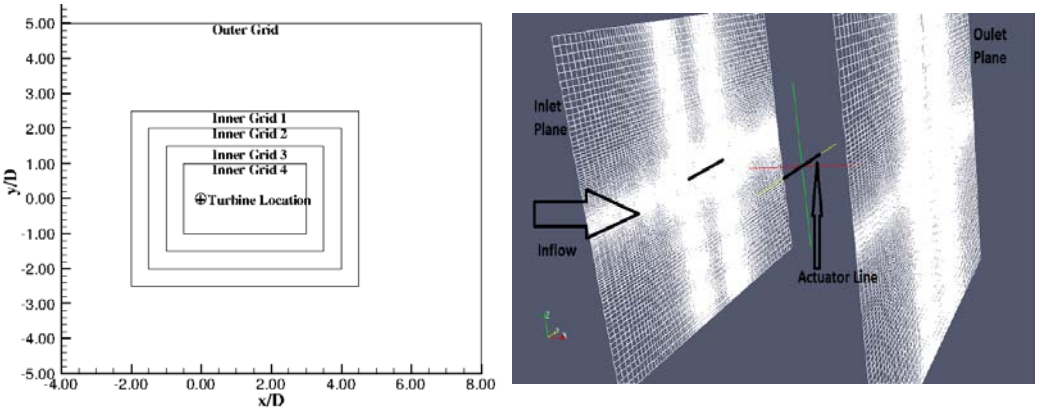

(a) **(b)**

Figure 4. An example of domain sizes and refinement levels for the non-stretched type of grid is shown in (a) planes of the stretched grid are shown in (b).

A. NREL Phase VI Rotor, $\varepsilon/\Delta r = const.$

Simulations were performed for the NREL Phase VI rotor under rotating and parked conditions. Table 1 comprises some blade and solver parameters. Note that the actuator width (or spacing) $\boldsymbol{\Delta b}$ was chosen slightly larger than the minimum grid spacing $\boldsymbol{\Delta r_{min}}$ so that the grid can distinguish between two adjacent actuator points. It has been found in previous studies that consistent results can be obtained for $\boldsymbol{\Delta b \leq \Delta r}$. Hence a further increase in the number of actuator points beyond this criterion is not worthwhile as it increases the cost of the ALM itself. The operating conditions and the simulation parameters for the NREL Phase VI rotor under rotating and parked conditions are presented in Table 2. Since the blades are not moving in the parked state, the time step Δt was chosen such that the wind traverses the same distance per time step as the blade tip under rotating conditions.

Table 1. Operating conditions and simulation parameters for the NREL Phase VI rotor.

	NREL Phase VI
Rotor Radius, R $(\boldsymbol{m})$	5.029
Wind Speed, $\boldsymbol{V_{wind}}$ $(\boldsymbol{m/s})$	7.0
Rot. Speed (RPM)	72.0
Time Period, T (sec)	0.833
Time Step, Δt = T/480 (sec)	0.00173611
$\boldsymbol{V_{tip}(m/s)}$	37.9178
$\boldsymbol{V_{tip}\Delta t}$ $\boldsymbol{(m)}$	0.0658
$\boldsymbol{\Delta r_{min}(m) \approx \Delta b\ (m)}$	0.17
Number of Actuator Points	27
Root Cutout, r/R	0.121

The ALM simulations for the rotating condition were performed with and without the Glauert[38] correction for computed blade loads. No Glauert correction was used for the parked condition. The Glauert correction accounts for root and tip losses and was originally developed for BEM-type computations of propeller loads. In general, there should be no reason to use the Glauert correction with the ALM since the 3-D flow field containing tip and root vortices is fully resolved. It is used here only as a means to demonstrate some shortcomings of the ALM when using $\boldsymbol{\varepsilon/\Delta r}$ = constant.

Table 2. Simulation parameters for NREL Phase VI rotor under rotating and parked conditions

NREL Phase VI Rotor	Rotating	Parked
Rated Wind Speed, $\boldsymbol{V_{wind}}$	7.0	20.1
Time Step, Δt (sec)	0.00174	0.00327
$\boldsymbol{V_{tip}\Delta t}$ or $\boldsymbol{V_{wind}\,\Delta t}$ (m)	0.0658	0.0658

A.1 Rotating Condition (72 RPM), V_{wind} = 7 m/s, $\boldsymbol{\varepsilon/\Delta r}$ = constant

Figures 5 and 6 show the spanwise variation of normal and tangential force coefficients, C_n and C_t, for the NREL Phase VI rotor at a wind speed of 7m/s where the flow is attached along the entire blade. A quantitative comparison with results obtained by XTurb-PSU and measured NREL data is also shown. Some of the discrepancy observed can be attributed to the particular choice of the Gaussian width, $\boldsymbol{\varepsilon}$. It can be noted from Table 3 that the predicted power increases with $\boldsymbol{\varepsilon}$. It is quite obvious, though, that the ALM seems to over-predict AOA and resultant blade loads near the root and tip. It is this overprediction of force that may result in overpredicted torque and hence power.

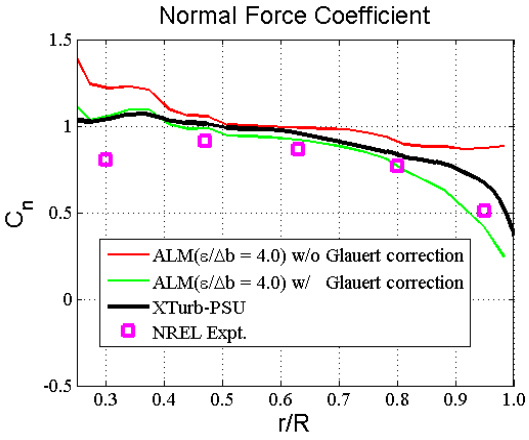

Figure 5. Spanwise variation of C_n for the NREL Phase VI rotor (V_{wind} = 7 m/s)

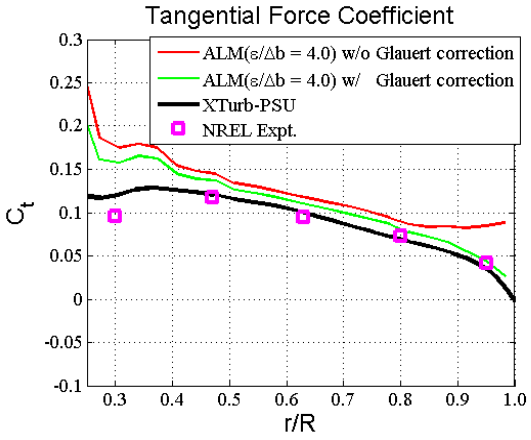

Figure 6. Spanwise variation of C_t for the NREL Phase VI rotor (V_{wind} = 7 m/s)

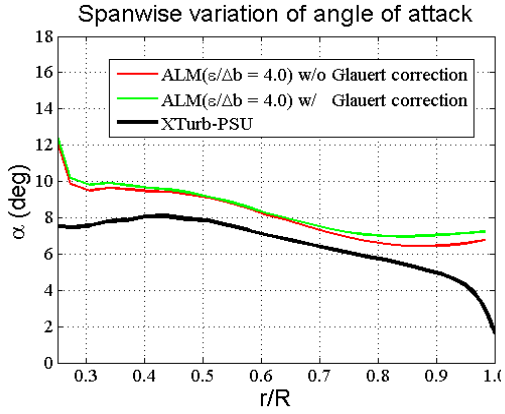

Figure 7. Spanwise variation of AOA for the NREL Phase VI rotor (V_{wind} = 7 m/s)

Table 3. Computed power and thrust for NREL Phase VI rotor (V_{wind} = 7 m/s)

NREL Phase VI Rotor	Power(W)	Thrust(N)
NREL Experiment	6030	1120
XTurb-PSU	6100	1240
ALM ($\boldsymbol{\varepsilon/\Delta b}$ = 4.0) [No correction]	7950	1450
ALM ($\boldsymbol{\varepsilon/\Delta b}$ = 2.0) [No correction]	7080	1380
ALM ($\boldsymbol{\varepsilon/\Delta b}$ = 4.0) [Glauert correction]	6450	1150
ALM ($\boldsymbol{\varepsilon/\Delta b}$ = 2.0) [Glauert correction]	5950	1120

Figure 7 shows the spanwise distribution of the local AOA, which is a good indicator to how well the local inflow conditions at the actuator line are predicted. It can be seen that the ALM over-predicts the local AOA towards the blade tips, which leads to the observed over-prediction of normal and tangential force coefficients in Figs 5-6. Results obtained by the Glauert correction in Figs. 5-6 actually under-predict the force coefficients considered when compared to NREL data and results obtained by XTurb-PSU. Though the Glauert correction produces better comparison with rotor power and thrust in Table 3 because of the modified aerodynamic force coefficients, it actually hardly affects AOA. The ultimate goal is to not use it in the simulations because i) it should not be necessary in a computed 3-D flow field, and ii) there is no equivalent correction factor that can be used in non-rotating (or parked) flow conditions.

A.2 Parked Condition, V_{wind} = 20.1 m/s, $\varepsilon/\Delta r$ = constant

Figures 8 and 9 show the spanwise variation of C_n and C_t for the NREL Phase VI rotor in a parked condition in comparison with NREL data and results obtained by XTurb-PSU. Improved agreement is observed when compared to the rotating case. Some discrepancy at the blade root and tip, however, persists. Comparing the plots for the rotating and parked conditions it is interesting to note that in the parked case both models and the data show excellent agreement in the middle part of the blade, while ALM computed force coefficients appear to be shifted for the rotating blade.

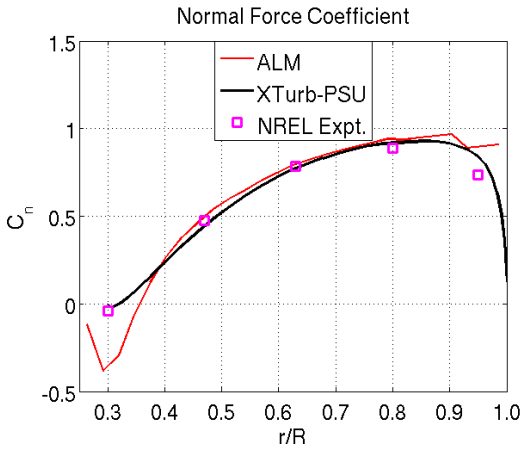

Figure 8. Spanwise variation of C_n for the NREL Phase VI rotor (Parked, V_{wind} = 20.1 m/s, $\varepsilon/\Delta b$ = 4.0)

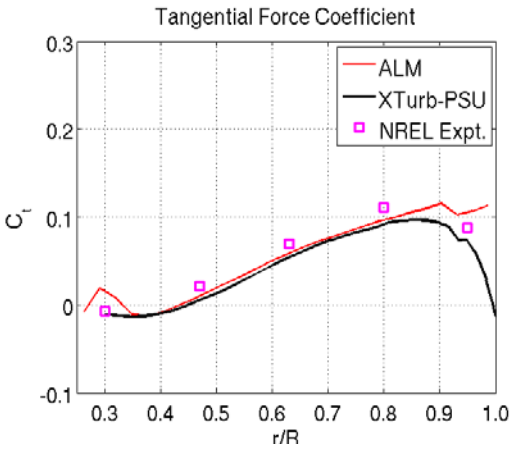

Figure 9. Spanwise variation of C_t for the NREL Phase VI rotor (Parked, V_{wind} = 20.1 m/s, $\varepsilon/\Delta b$ = 4.0)

The same can be observed for the spanwise AOA distribution in Fig. 10. Up to this point, there are strong indications that the present ALM does not predict accurately the flow conditions and loads near the blade root and tip for a constant Gaussian spreading width ε for both rotating and parked conditions. The exact reason for this is unclear at present, however one can surmise that it must be related to the facts that the volumetric body-force spreading acts beyond the geometric blade edges and that the strong force gradients near the blade tip, for example, are alleviated by the force spreading at more inboard stations (e.g. 90% R) that leads to a higher-than-expected force very close to the actual blade tip. This is further supported by the following analyses involving two different wing designs both with an elliptical load distribution.

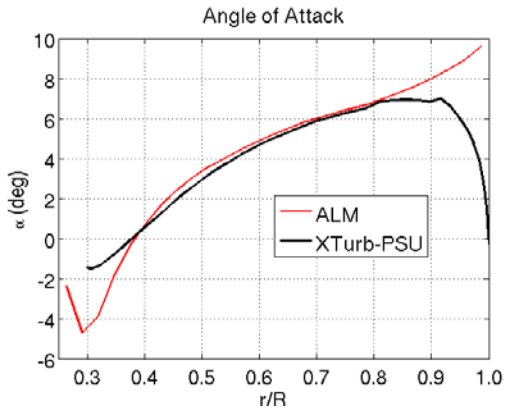

Figure 10. Spanwise variation of AOA for the NREL Phase VI rotor (Parked, V_{wind} = 20.1 m/s, $\varepsilon/\Delta b$ = 4.0)

B. Elliptically Loaded Wing at V_{wind} = 20.1 m/s, $\varepsilon/\Delta r$ = constant

The elliptically loaded wing is a classical optimal case in applied aerodynamics. In order to test the ALM, a wing with an elliptic planform was designed that has the same wing area (***3.066*** $\boldsymbol{m^2}$) and aspect ratio (***8.249***) as the NREL Phase VI rotor blade whose near-root cylindrical section (r/R < 0.25) is replaced by an extrapolation of the aerodynamic part. An illustration is given in Figure 11. In this case, 41 actuator points were used along the actuator line. The Gaussian spreading width $\boldsymbol{\varepsilon}$ was chosen to be about four times the actuator spacing $\boldsymbol{\Delta b}$ as a baseline test case. The wing is exclusively equipped with the S809 airfoil. The geometric AOA was set to be ***8***° leading to a mid-span circulation (Γ_0) of ***6.6816*** m^2/s and an induced AOA (α_i) of ***1.8936***° according to finite-wing theory. Two wings were designed with one being untwisted and having an elliptic planform (or chord) distribution, while the second one has a rectangular planform (constant chord) and is twisted such that it produces an elliptic lift distribution at a geometric AOA of ***8***°. Table 4 summarizes some of the geometric parameters and solver settings.

Table 4. Details of the wing designs with elliptical load distribution

Planform	Elliptic	Rectangular
Span ($\boldsymbol{m}$)	5.029	5.029
Area ($\boldsymbol{m^2}$)	3.066	3.066
Aspect Ratio	8.249	8.249
Mid-Chord (m)	0.7763	0.6096
Wind Speed, $\boldsymbol{V_{wind}}$ ($\boldsymbol{m/s}$)	20.1	20.1
Time Step, Δt (sec)	0.0033	0.0033
$\boldsymbol{V_{wind}\Delta t}$ ($\boldsymbol{m}$)	0.0658	0.0658
$\boldsymbol{\Delta r_{min}}$($\boldsymbol{m}$)	0.11	0.11
Number of Actuator Points	41	41
Actuator Width, $\boldsymbol{\Delta b}$ ($\boldsymbol{m}$)	0.1226	0.1226

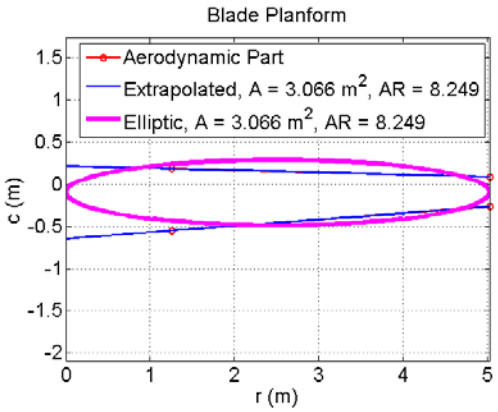

Figure 11. Wing with elliptic planform designed for analysis

B.1 Elliptically Loaded Wing at V_{wind} = 20.1 m/s (Elliptic Planform) , $\varepsilon/\Delta r$ = constant

Classical lifting-line theory thus suggests a constant effective AOA of ***6.1064***° along the wing span. Figures 12, 14 and 15 show the spanwise variation of AOA, C_n and C_t, respectively, for the designed elliptic wing planform. The results from XTurb-PSU match well with the theory as expected from a lifting-line model. The ALM predictions exhibit quite large discrepancies when compared to XTurb-PSU and the theoretical results. It can also be observed that as $\boldsymbol{\varepsilon}$ decreases the predicted AOA decreases, and the strong deviation from the theoretical results near the wing tips occurs over a smaller portion of the wing.

B.2 Elliptically Loaded Wing at V_{wind} = 20.1 m/s (Rectangular Planform) , $\varepsilon/\Delta r$ = constant

The blade twist of the rectangular wing was designed with the exact same elliptic circulation distribution as for the wing with elliptic planform described above. Figures 13, 16 and 17 show the spanwise variation of AOA, C_n and C_t, respectively, for the wing with rectangular planform and elliptical loading. The results from XTurb-PSU match again well with the theory with small deviations. This can be attributed to non-zero drag values used in the S809 polar. The ALM predictions of AOA are close to the theory and XTurb-PSU results except at the wing tips. The force coefficients predicted by ALM exhibit some deviation compared to those computed by XTurb-PSU.

The previous observation that AOA and blade tip loads are over-predicted for $\boldsymbol{\varepsilon/\Delta r}$ = constant holds true for both the wing designs.

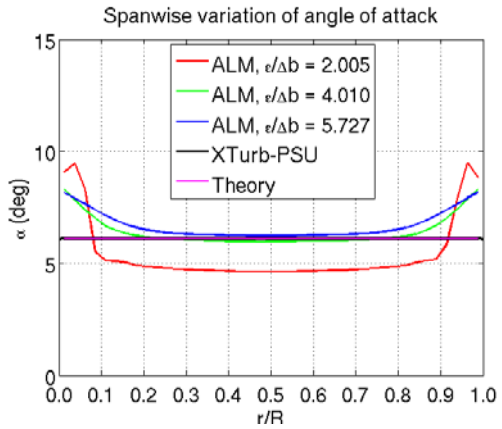

Figure 12. Spanwise variation of AOA (Elliptic planform, V_{wind} = 20.1 m/s)

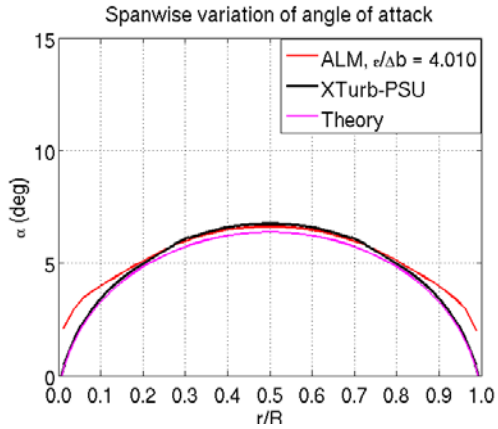

Figure 13. Spanwise variation of AOA (Rectangular planform, V_{wind} = 20.1 m/s)

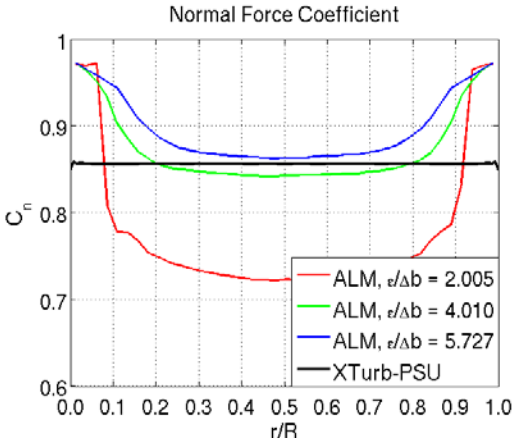

Figure 14. Spanwise variation of C_n (Elliptic planform, V_{wind} = 20.1 m/s)

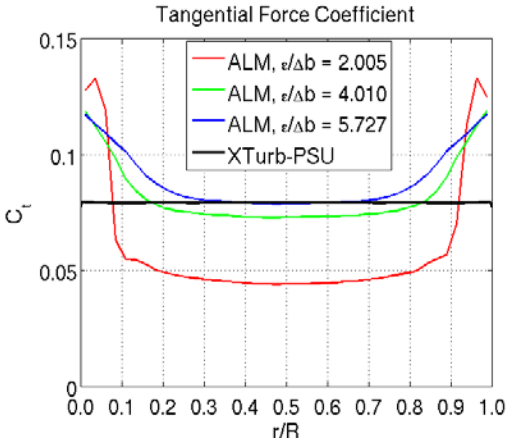

Figure 15. Spanwise variation of C_t (Elliptic planform, V_{wind} = 20.1 m/s)

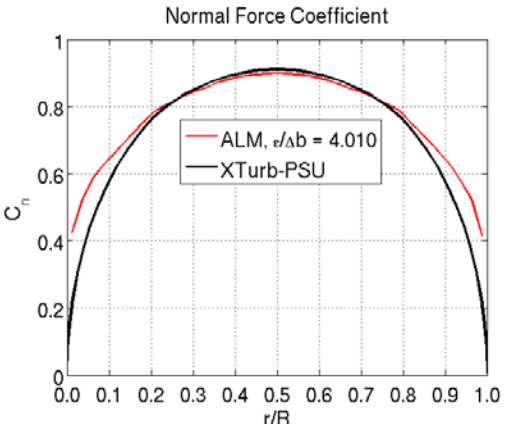

Figure 16. Spanwise variation of C_n (Rectangular planform, V_{wind} = 20.1 m/s)

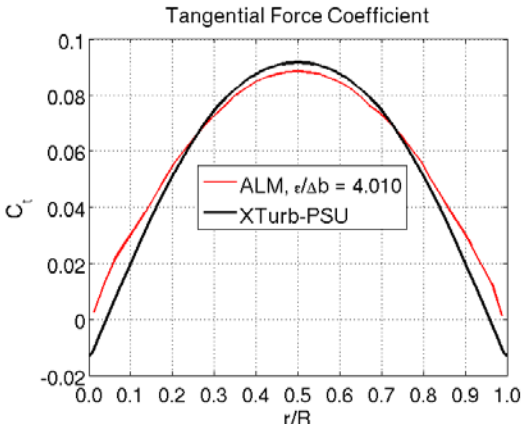

Figure 17. Spanwise variation of C_t (Rectangular planform, V_{wind} = 20.1 m/s)

C. NREL Phase VI Rotor, $\boldsymbol{\varepsilon/c^*}$= constant

In this section, the new method described in section II.A.3 for a variable Gaussian spreading width $\boldsymbol{\varepsilon}$ is tested for the NREL Phase VI rotor. Given an aspect ratio of $\boldsymbol{AR}$ = **10.455** for the blade from Fig. 3a, the $\boldsymbol{\varepsilon/c^*}$ criterion in Equation (9b) for the fictitious elliptic planform $\boldsymbol{c^*}$ can be computed for $\boldsymbol{\Delta r}$ and $\boldsymbol{R}$ from Table 1 and by choosing a user-specified $\boldsymbol{n_{max}}$. In this work, we considered $\boldsymbol{n_{max} = 4}$ $(\boldsymbol{\varepsilon/c^* = 1.0 * \Delta r * \pi *}$ AR/b) and $\boldsymbol{n_{max} = 3}$ $(\boldsymbol{\varepsilon/c^* = 0.75 * \Delta r * \pi *}$ AR/b) along with $\boldsymbol{n_{min} = 0, 1, 2}$. Table 5 comprises the parameters associated with the test cases for the problem under consideration. For comparison with the results for the methods in II.A.1 and II.A.2, the relevant parameters are also presented. The same set of parameters has been used for both rotating and parked conditions. The integrated values of thrust and power, after the solutions become stationary, have also been documented for each of these cases for the rotating condition and are presented in Table 5.

Table 5: Parameters for constant and variable Gaussian spreading width for NREL Phase VI rotor (Actual planform as well as fictitious elliptic planform)

$\boldsymbol{\varepsilon}$ - Method	Fictitious Chord, $\boldsymbol{c_0}$ *(m)*	Grid Resolution, $\boldsymbol{\Delta r}$ *(m)*	$\boldsymbol{n_{max}}$	$\boldsymbol{n_{min}}$	$\boldsymbol{\varepsilon}$ *(m)*	$\boldsymbol{\varepsilon/c^*}$ *or* $\boldsymbol{\varepsilon/c}$	$\boldsymbol{\varepsilon_{R/2}}$ *(m)* *or* $\boldsymbol{\varepsilon_{min}}$*(m)*	Integrated Thrust *(N)*	Integrated Power *(W)*
II.A.1	NA	0.17	NA	NA	0.7025	≠ const.	0.7025	1450	7950
II.A.2	NA	0.17	4	1	≠ const.	1.1103	0.1750	1425	7640
II.A.3	0.6124	0.17	4	2	≠ const.	1.1103	0.3500	1415	7545
	0.6124	0.17	4	1	≠ const.	1.1103	0.1750	1395	7350
	0.6124	0.17	4	0	≠ const.	1.1103	0.0000	1390	7340
	0.6124	0.17	3	1	≠ const.	0.8327	0.1750	1365	6970

C.1 Rotating Condition (72 RPM), V_{wind} = 7 m/s, $\boldsymbol{\varepsilon/c^*}$= constant

The results obtained for the proposed method described in II.A.1-II.A.3 are presented below for the NREL Phase VI rotor. Figures 18, 19 and 20 show the spanwise variation of AOA, C_n and C_t. It can be observed that compared to the case of $\boldsymbol{\varepsilon/\Delta r}$ = constant, $\boldsymbol{\varepsilon/c}$ = constant (with actual planform) produces slightly better results. However, it is the $\boldsymbol{\varepsilon/c *}$ = constant case that produces substantially better results, particularly for the tip loads. It is worth noting that the Glauert correction is not needed to obtain improved results for the blade tip loads. Comparing the various cases for the proposed methods, it appears that $\boldsymbol{n_{max}}$**= 3** and $\boldsymbol{n_{min}}$= 1 work quite well for the rotating case.

Apart from the sectional loads, the integrated thrust and power were also analyzed. It can be noted from Table 5 that the new method alleviates the over-prediction of thrust and power. The integrated thrust and power for $\boldsymbol{n_{max}}$**= 3** and $\boldsymbol{n_{min}}$= 1 are 1365 N and 6970 W respectively. These values are much closer to the measured data, as listed in Table 3, compared to when a constant $\boldsymbol{\varepsilon/\Delta r}$ is used.

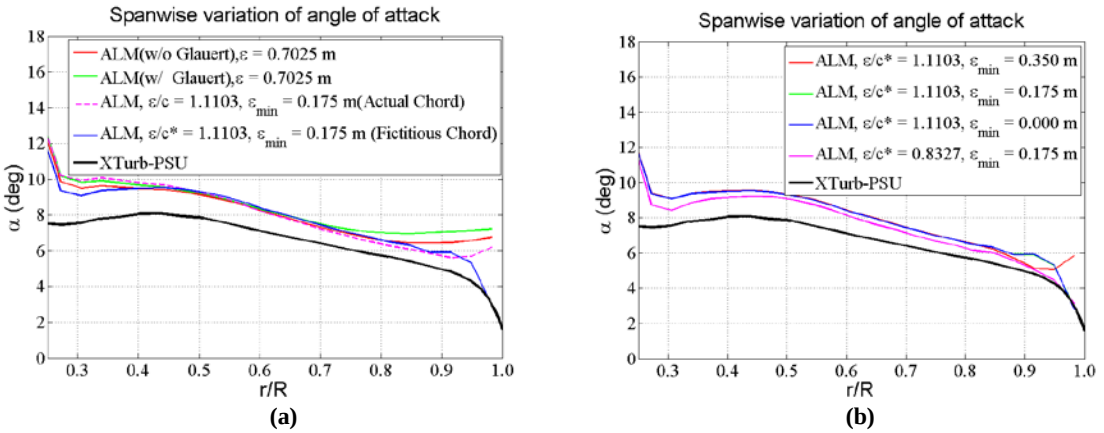

(a) **(b)**

Figure 18. Spanwise variation of AOA for the NREL Phase VI rotor (V_{wind} = 7 m/s, ε/c=const. or ε/c*=const.)

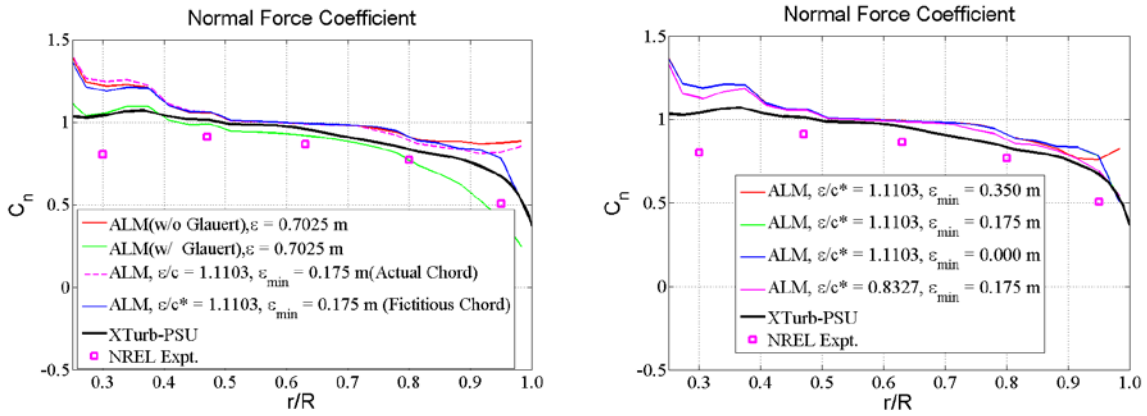

(a) **(b)**

Figure 19. Spanwise variation of C_n for the NREL Phase VI rotor (V_{wind} = 7 m/s, ε/c=const. or ε/c*=const.)

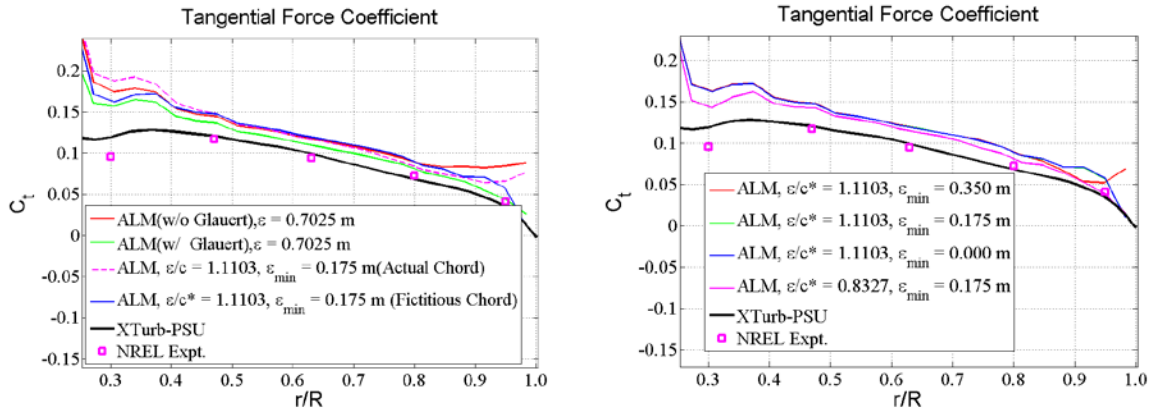

(a) **(b)**

Figure 20. Spanwise variation of C_t for the NREL Phase VI rotor (V_{wind} = 7 m/s, ε/c=const. or ε/c*=const.)

C.2 Parked Condition, V_{wind} = 20.1 m/s, ε/c^*= constant

The results for the NREL Phase VI rotor under parked conditions are presented below. Figures 21, 22 and 23 show the spanwise variation of AOA, C_n and C_t. The observations here are similar to those made for the rotating case. It can be noticed that the proposed method produces improved results and that n_{max}= 3 and n_{min}= 1 work again well for the parked case.

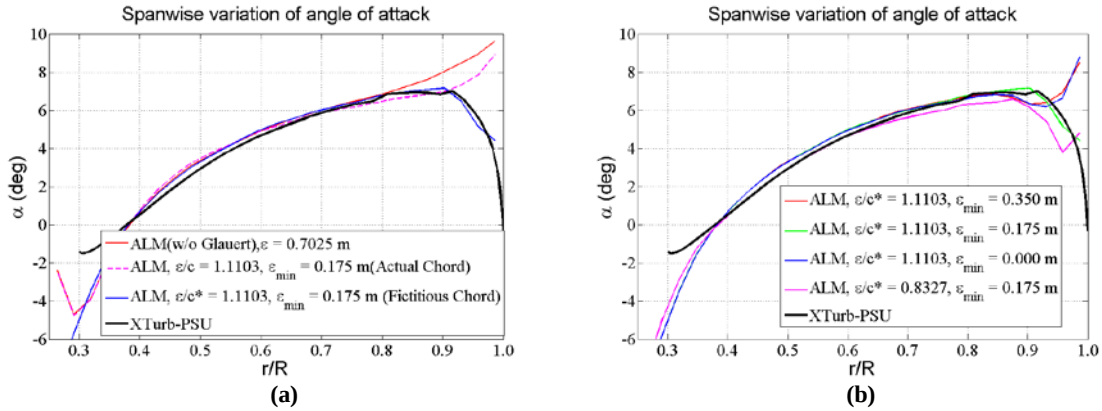

(a) **(b)**

Figure 21. Spanwise variation of AOA for the NREL Phase VI rotor (Parked**, ε/c*=const.)**

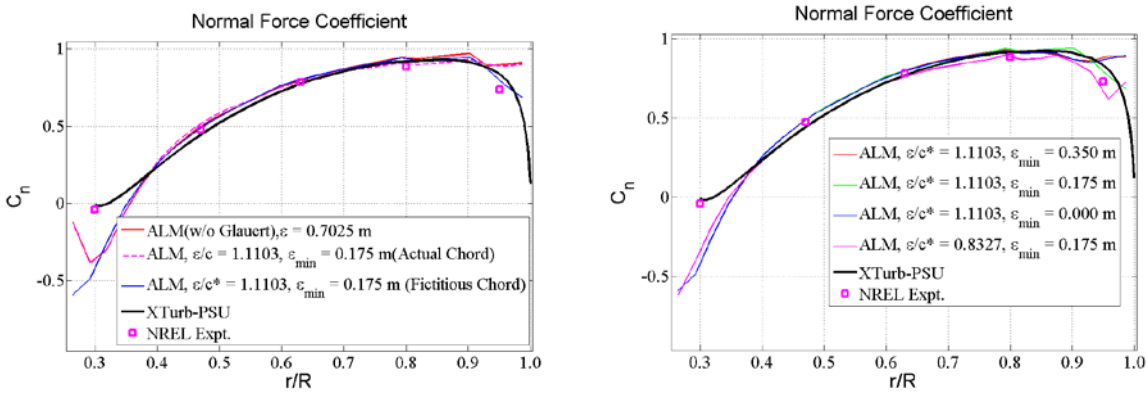

(a) **(b)**

Figure 22. Spanwise variation of C_n for the NREL Phase VI rotor (Parked**, ε/c*=const.)**

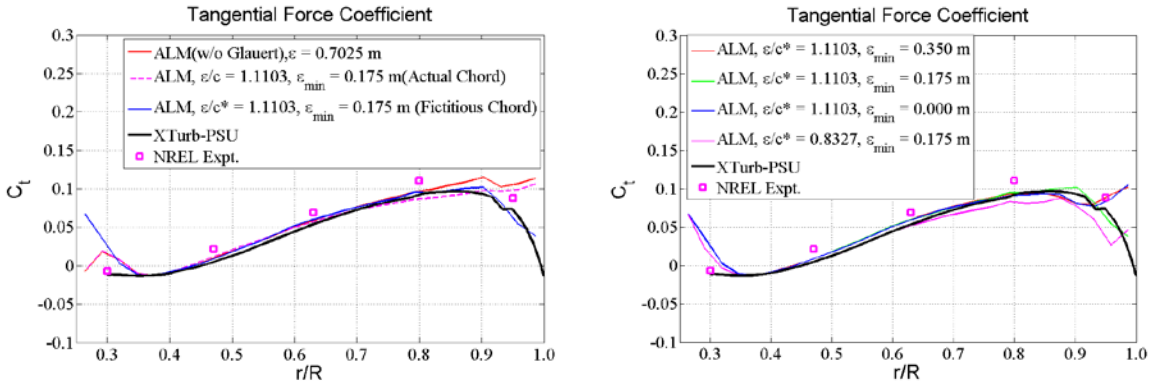

(a) **(b)**

Figure 23. Spanwise variation of C_t for the NREL Phase VI rotor (Parked**, ε/c*=const.)**

D. Elliptically Loaded Wing at V_{wind} = 20.1 m/s, ε/c^* = constant

Having observed that the proposed method described in section II.A.3 for a variable Gaussian spreading width $\boldsymbol{\varepsilon}$ shows improved results for the NREL Phase VI rotor, the classical aerodynamics problem of an elliptically loaded wing was studied with the newly proposed spreading method. Here only the elliptic planform was considered as the rectangular planform of the same AR results in the same fictitious elliptic planform $\boldsymbol{c}^*$. The criterion in Equation (9b) for the fictitious elliptic planform $\boldsymbol{c}^*$ can be computed in the same manner as for NREL Phase VI rotor. Table 6 comprises the parameters associated with the test cases.

Table 6: Parameters for constant and variable Gaussian spreading width for an elliptically loaded wing (elliptical planform, uniform grid)

ε - Method	Fictitious Chord, c_0 (m)	Grid Resolution, Δr (m)	n_{max}	n_{min}	ε (m)	ε/c^* or ε/c	$\varepsilon_{R/2}$ (m) or ε_{min}(m)
II.A.1	NA	0.1118	NA	NA	0.5026	≠ const.	0.5026
II.A.3	0.7762	0.1118	4	2	≠ const.	0.5761	0.2300
	0.7762	0.1118	4	1	≠ const.	0.5761	0.1150
	0.7762	0.1118	4	0	≠ const.	0.5761	0.0000
	0.7762	0.1118	3	1	≠ const.	0.4321	0.1150

Figures 24, 25 and 26 show the spanwise variation of AOA, C_n and $C_t$obtained on a uniform grid described in section II. It can be observed that, compared to the case of $\boldsymbol{\varepsilon/\Delta r}$ = constant, the cases with $\boldsymbol{\varepsilon/c*}$ = constant show an under-prediction of the blade tip loads except for one case. Comparing the various cases for the proposed method, it appears that $\boldsymbol{n_{max}}$**= 4** and $\boldsymbol{n_{min}}$= 1 work quite well for the wing. It can also be seen that $\boldsymbol{n_{max}}$**= 4** and $\boldsymbol{n_{min}}$= 0 leads to some instability.

Figures 27, 28 and 29 show the spanwise variation of AOA, C_n and C_t for the elliptic wing problem using a stretched grid. The grid used had a smallest resolution of 1% of span (***0.05029 m***) with the refined region around the actuator line and near the tips extending over 20% span. An expansion factor of 1.05 was used. The resulting radial spacing was ***0.1242 m*** at the mid-span. Table 7 comprises the parameters associated with the test cases for the stretched grid. Considering the resolutions at the tip as well as mid-span, the $\boldsymbol{\varepsilon/c}*$ criterion in Equation (9b) was computed with $\boldsymbol{n_{max}}$**= 4** and $\boldsymbol{n_{min}}$**=** 1. The cases for $\boldsymbol{\varepsilon/\Delta r}$ = constant were also considered for comparison. The Gaussian spreading width $\boldsymbol{\varepsilon}$ was chosen such that $\boldsymbol{\varepsilon/c_0}$ was the same as $\boldsymbol{\varepsilon/c}*$ from above for each of the two grid resolutions considered. Comparing the various cases for the proposed method, it appears that $\boldsymbol{n_{max}}$**= 4** and $\boldsymbol{n_{min}}$**=** 1 along with the $\boldsymbol{\varepsilon/c}*$ criterion based on the grid resolution at the mid-span produces the best result. Thus, it can be concluded that grid stretching has a positive effect on the computed inflow distribution.

Table 7: Parameters for constant and variable Gaussian spreading width for an elliptically loaded wing (elliptical planform, stretched grid)

ε - Method	Fictitious Chord, c_0 (m)	Grid Resolution, Δr (m)	n_{max}	n_{min}	ε (m)	ε/c^* or ε/c	$\varepsilon_{R/2}$ (m) or ε_{min}(m)
II.A.1	NA	0.05029	NA	NA	0.2011	≠ const.	0.2011
	NA	0.12420	NA	NA	0.4968	≠ const.	0.4968
II.A.3	0.7762	0.05029	4	1	≠ const	0.2591	0.0500
	0.7762	0.12420	4	1	≠ const	0.6400	0.1250

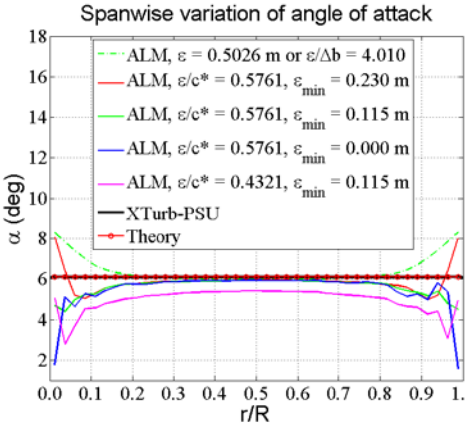

Figure 24. Spanwise variation of AOA (Elliptic planform, V_{wind} = 20.1 m/s, ε/c*=const.)

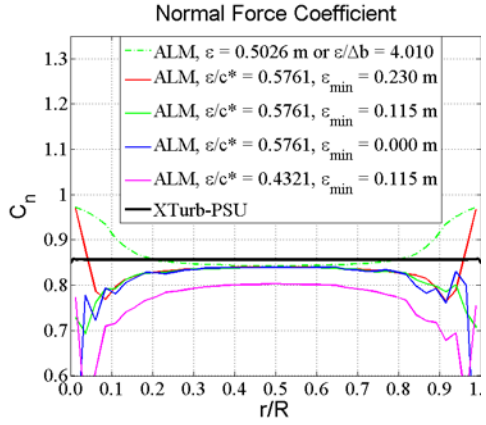

Figure 25. Spanwise variation of C_n (Elliptic planform, V_{wind} = 20.1 m/s, ε/c*=const.)

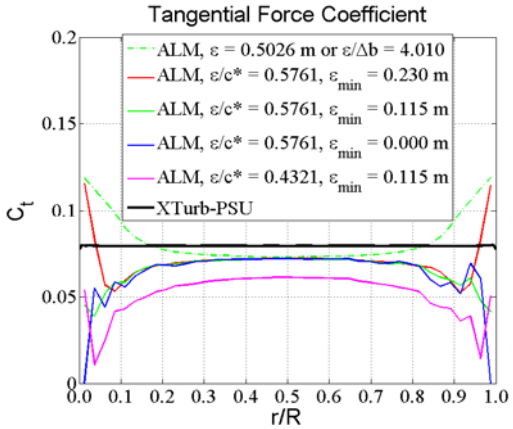

Figure 26. Spanwise variation of C_t (Elliptic planform, V_{wind} = 20.1 m/s, ε/c*=const.)

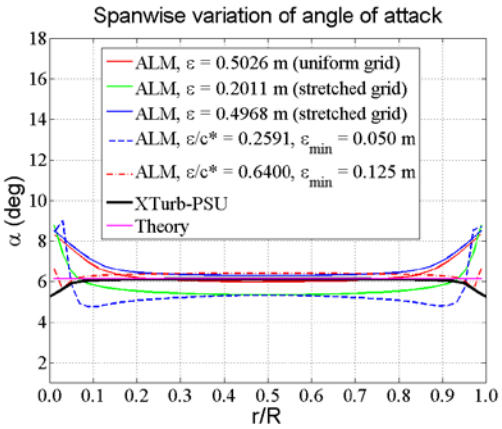

Figure 27. Spanwise variation of AOA (Elliptic planform, V_{wind} = 20.1 m/s, ε/c*=const.) Stretched grid

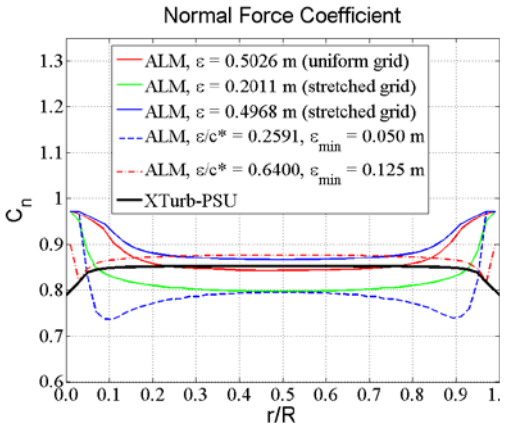

Figure 28. Spanwise variation of C_n (Elliptic planform, V_{wind} = 20.1 m/s, ε/c*=const.) Stretched grid

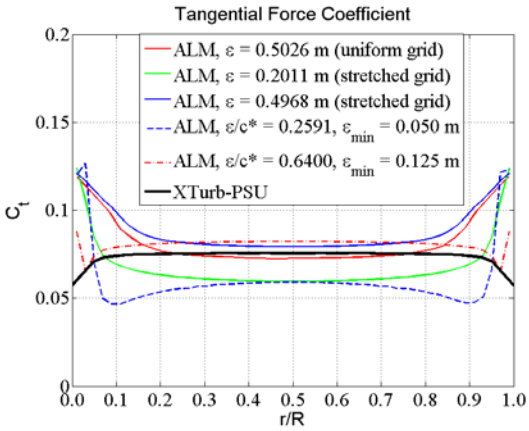

Figure 29. Spanwise variation of C_t (Elliptic planform, V_{wind} = 20.1 m/s, ε/c*=const.) Stretched grid

E. NREL 5-MW turbine at V_{wind} = 8 m/s, ε/c^* = constant

It was noted that the method described in section II.A.3 for a variable Gaussian spreading width $\boldsymbol{\varepsilon}$ shows improved results for the NREL Phase VI rotor as well as elliptically loaded wing both with a uniform and a stretched grid. The $\boldsymbol{\varepsilon/c^*}$ criterion in Equation (9b) was computed in a similar manner for the NREL 5-MW turbine. Table 8 comprises the parameters associated with the test cases for the problem under consideration. The operating conditions for the NREL 5-MW turbine are presented in Table 9.

Figures 30, 31 and 32 show the spanwise variation of AOA, C_n and C_t. Only a uniform grid was used for the simulations. Here also, compared to the case of $\boldsymbol{\varepsilon/\Delta r}$ = constant, the cases of $\boldsymbol{\varepsilon/c*}$ = constant produce better results, particularly for the tip loads. Comparing the various cases for the proposed method, it appears that $\boldsymbol{n_{max}}$**= 4** and $\boldsymbol{n_{min}}$**=** 1 work quite well. Integrated power and thrust are also documented for the sake of completeness.

The observations suggest that the proposed method in II.A.3 can be applied to a utility-scale turbine as well.

Table 8: Parameters for constant and variable Gaussian spreading width for NREL 5-MW turbine (Actual planform as well as fictitious elliptic planform)

ε - Method	Fictitious Chord, c_0 (m)	Grid Resolution, Δr (m)	n_{max}	n_{min}	ε (m)	ε/c^* or ε/c	$\varepsilon_{R/2}$ (m) or ε_{min}(m)	Integrated Thrust (kN)	Integrated Power (kW)
II.A.1	NA	1.96875	NA	NA	3.93750	≠ const.	3.93750	390	1970
II.A.3	4.4376	1.96875	4	2	≠ const.	1.7746	3.93750	409	2110
	4.4376	1.96875	4	1	≠ const.	1.7746	1.96875	425	2165
	4.4376	1.96875	4	0	≠ const.	1.7746	0.00000	416	2150
	4.4376	1.96875	3	1	≠ const.	1.3309	1.96875	400	2035

Table 9. Operating conditions and simulation parameters for the NREL Phase VI rotor.

	NREL Phase VI
Rotor Radius, R (m)	63
Wind Speed, V_{wind} (m/s)	8.0
Rot. Speed (RPM)	9.156
Time Period, T (sec)	6.55
Time Step, Δt (sec)	0.03
$V_{tip}(m/s)$	60.4052
$V_{tip}\Delta t$ (m)	1.8122
$\Delta r_{min}(m)$	1.96875
Number of Actuator Points	64
Root Cutout, r/R	0.1

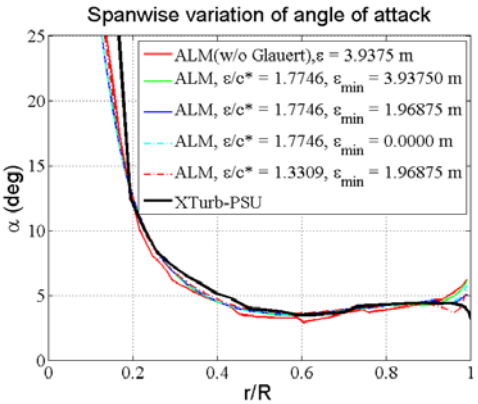

Figure 30. Spanwise variation of AOA (NREL 5-MW turbine, V_{wind} = 8 m/s, ε/c*=const.)

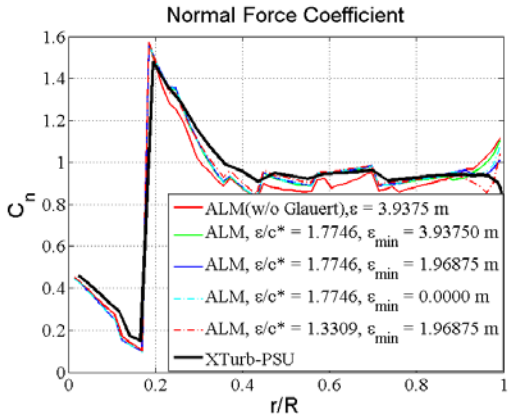

Figure 31. Spanwise variation of C_n (NREL 5-MW turbine, V_{wind} = 8 m/s, ε/c*=const.)

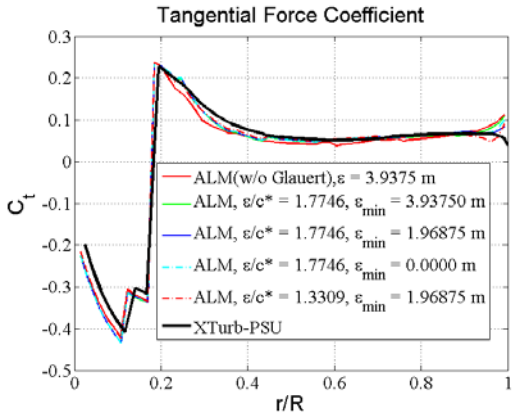

Figure 32. Spanwise variation of C_t (NREL 5-MW turbine, V_{wind} = 8 m/s, ε/c*=const.)

IV. Summary and Conclusions

The objective of this work was to assess and improve the accuracy of the state-of-the-art actuator-line method ALM in predicting rotor blade loads. The ALM was applied within an OpenFOAM computational fluid dynamics (CFD) solver to various blade planform geometries including the NREL Phase VI rotor in rotating and parked conditions, two wing designs with an elliptic load distribution, and the NREL 5-MW turbine. Results obtained for sectional AOA as well as normal and tangential force coefficients were compared to data, when available, and to results obtained by the wind turbine design and analysis code XTurb-PSU.

It was found that the current ALM shows a consistent overprediction in rotor tip loads for all blade planforms considered when using a constant spreading radius (or width) $\boldsymbol{\varepsilon/\Delta r = const.}$ of the Gaussian within the ALM discretization. Consequently, integrated rotor thrust and power (or torque) are overpredicted accordingly, which is likely to have an effect on the recovery process of the wake momentum deficit in the rotor wake, which will be a subject of future studies. Furthermore, it was noted that increasing the constant $\boldsymbol{\varepsilon/\Delta r}$ further increases the integrated rotor loads. A new method was developed for a variable spreading width $\boldsymbol{\varepsilon}$ along the blade span that is based on a 'fictitious' elliptic planform $\boldsymbol{c^*}$ with the same aspect ratio $\boldsymbol{AR}$ as the actual blade. The proposed $\boldsymbol{\varepsilon/c^* = const.}$ criterion is a function of the blade $\boldsymbol{AR}$, the grid resolution $\boldsymbol{\Delta r/R}$, and free parameters $\boldsymbol{n_{max}}$ and $\boldsymbol{n_{min}}$ that describe the maximum and minimum spreading with at the mid-blade and tip locations, respectively, in multiples of the grid spacing $\boldsymbol{\Delta r}$ along the blade. It was demonstrated that the proposed $\boldsymbol{\varepsilon/c^* = const.}$ criterion gives improved predictions of computed rotor loads for all blade designs considered. In addition, choosing $\boldsymbol{n_{max} = 3,4}$ and $\boldsymbol{n_{min} = 1}$ consistently gave the best predictions for all cases. A stretched grid with refinement at the blade tips of about $\boldsymbol{\Delta r/R = 0.01}$ further improved the prediction of the local inflow in terms of AOA.

V. References

[1] "20% Wind Energy by 2030," US Department of Energy Executive summary, DOE/GO-102008-2578, December 2008.

[2] "Eastern Wind Integration and Transmission Study," prepared for the National Renewable Energy Laboratory by the EnerNex Corporation, NREL/SR-5500-47078, February 2011.

[3] "Western Wind and Solar Integration Study," prepared for the National Renewable Energy Laboratory by GE Energy, NREL/SR-550-47434, May 2010.

[4] Katic, I., Hoejstrup, J., Jensen, N. O., "A Simple Model for Cluster Efficiency," *Proceedings of the European Wind Energy Association*, Rome, Italy, 1986.

[5] Rathmann, O., Frandsen, S. T., Barthelmie, R. J., "Wake Modelling for Intermediate and Large Wind Farms," *Proceedings of the European Wind Energy Conference and Exhibition*, Milan, Italy, 2007.

[6] "WAsP – The Wind Atlas Analysis and Application Program," *Risoe National Laboratory for Sustainable Energy*, Roskilde, Denmark. [Online]. Available: http://www.wasp.dk/Products/WAsP.html [Accessed July 17th 2011].

[7] Crespo, A., Hernandez, J., Fraga, E., Andreu, C., "Experimental validation of the UPM computer code to calculate wind turbine wakes and comparison with other models," *Journal of Wind Engineering and Industrial Aerodynamics*, **27**, 77-88, 1988
[8] Hassan, U. A., "A Wind Tunnel Investigation of the Wake Structure within Small Wind Turbine Farms," Rep. ETSU WN 5113, 1993.
[9] Sørensen, J. N., Shen, W. Z., Munduate, X., "Analysis of Wake States by a Full-Field Actuator Disc Model," *Int. J. Numer. Meth. Fl.*, **1**, 73-78, 1998.
[10] Leclerc, C., Masson, C., "Toward Blade-Tip Vortex Simulation with an Actuator-Lifting Surface Model," *AIAA-2004-0667*, 2004.
[11] Leclerc, C., Masson, C., "Wind Turbine Performance Predictions Using a Differential Actuator-Lifting Disk Model," *J. Sol. Energ.Engin. Transactions of the ASME*, **127**, 200-208, 2005.
[12] Réthoré, P. E., Sørensen, N. N., Zahle, F., "Validation of an Actuator Disc Model," EWEC, 2010.
[13] Mikkelsen, R., "Actuator Disc Methods Applied to Wind Turbines. Technical University of Denmark," PhD Thesis, 2003.
[14] Lu, H., Porté-Agel, F., "Large-Eddy Simulation of a Very Large Wind Farm in a Stable Atmospheric Boundary Layer," *Physics of Fluids*, **23**, 065101, 2011.
[15] Ivanell, S., Mikkelsen, R., Sørensen, J., Henningson, D., "ACD Modelling of Wake Interaction in the Horns Rev Wind Farm," In *Extended Abstracts for Euromech Colloquim 508 on Wind Turbine Wakes*, European Mechanics Society, Madrid, Spain, 2009.
[16] Meyers, J., Meneveau, C., "Large Eddy Simulations of Large Wind-Turbine Arrays in the Atmospheric Boundary Layer," *AIAA-2010-0827*, 2010.
[17] Singer, M., Mirocha, J., Lundquist, J., Cleve, J. "Implementation and assessment of turbine wake models in the Weather Research and Forecasting model for both mesoscale and large-eddy simulation," 2010.
[18] Conzemius, B., Lu, H., Chamorro, L., Wu, Y.-T., Porte-Agel, F. "Development and testing of a 21 wind farm simulator at an operating wind farm," *Presentation from AWEA 2010 WindPower Conference and Exhibition*, Dallas, TX.
[19] Stovall, T. D., Pawlas, G., Moriarty, P. J., "Wind farm wake simualtions in OpenFOAM," *AIAA-2010-0825*, 2010.
[20] Sørensen, J. N., Shen, W. Z., "Numerical modeling of Wind Turbine Wakes," *ASME Journal of Fluids Engineering*, **124**, 393-399, 2002.
[21] Troldborg, N., Sørensen, J. N., Mikkelsen, R., "Actuator Line Simulation of Wake of Wind Turbine Operating in Turbulent Inflow," *Journal of Physics: Conference Series, The Science of Making Torque from Wind*, Technical University of Denmark, Lyngby, Denmark, 2007.
[22] Troldborg, N., "Actuator Line Modeling of Wind Turbine Wakes," Technical University of Denmark, PhD Thesis, 2008.
[23] Troldborg, N., Sørensen, J., Mikkelsen, R., "Numerical Simulations of Wake Characteristics of a Wind Turbine in Uniform Flow," *Wind Energy*, **13**, 86-99, 2010.
[24] Sibuet Watters, C., Masson, C., "Modelling of Lifting-Device Aerodynamics Using the Actuator Surface Concept," *Int. J. Numer. Meth. Fl.*, **62**(11), 1264-1298, 2010.
[25] Dobrev, I., Massouh, F., Rapin, M., "Actuator surface hybrid model," *Journal of Physics Conference Series, The Science of Making Torque from Wind*, Technical University of Denmark, Lyngby, Denmark, 2007.
[26] Shen, W. Z., Zhang, J. H., Sorensen, J. N., "The Actuator Surface Model: A New Navier-Stokes Based Model for Rotor Computations," *J. Sol. Energy Eng. Trans. ASME*, **131**(1), doi:10.1115/1.3027502., 2009.
[27] OpenFOAM, Ver. 2.0.x, [available online] ESI Group-OpenCFD, URL: http:// www.openfoam.org/git.php [accessed 13 December 2012].
[28] Churchfield, M. J., Moriarty, P. J., Vijayakumar, G., Brasseur, J., "Wind Energy-Related Atmospheric Boundary-Layer Large-Eddy Simulation Using OpenFOAM," *NREL/CP-500-48905*, 2010.
[29] Churchfield, M. J., "Wind Energy / Atmospheric Boundary Layer Tools and Tutorials," *Training Session at the 6th OpenFOAM Workshop*, The Pennsylvania State University, 2011.
[30] Churchfield, Matthew J., Lee, S., Moriarty, Patrick J., Martínez, Luis A., Leonardi, S., Vijayakumar, G. and Brasseur, J. G., "A Large-Eddy Simulation of Wind-Plant Aerodynamics," *AIAA 2012-0537*, Nashville, TN.
[31] Churchfield, Matthew J., Lee, S., Michalakes, J., and Moriarty, Patrick J., "A Numerical Study of the Effects of Atmospheric and Wake Turbulence on Wind Turbine Dynamics," *Journal of Turbulence*, Vol. 13, No. 12, 2012.
[32] Jha, Pankaj K., Brillembourg, D., and Schmitz, S., "Wind Turbines under Atmospheric Icing Conditions - Ice Accretion Modeling, Aerodynamics, and Control Strategies for Mitigating Performance Degradation," *AIAA 2012-1287-868*, 50th AIAA Aerospace Sciences Meeting, 09 - 12 January 2012, Nashville, TN.
[33] Martínez, Luis A., Leonardi, S., Churchfield, Matthew J., and Moriarty, Patrick J., "A Comparison of Actuator Disk and Actuator Line Wind Turbine Models and Best Practices for Their Use," *AIAA 2012-0900*, Nashville, TN.

[34] Moriarty, P.J. and Hansen, A.C., "AeroDyn Theory Manual," NREL/TP-500-36881, January 2005, URL: http://www.nrel.gov/docs/fy05osti/36881.pdf.
[35] Chattot, J.J., "Design and Analysis of Wind Turbines Using Helicoidal Vortex Model," *Computational Fluid Dynamics Journal*, Vol. 11, No. 1, April 2002, pp. 50-54.
[36] Du, Z. and Selig, M.S., "A 3-D Stall-Delay Model for Horizontal Axis Wind Turbine Performance Prediction," AIAA-98-0021, *36th AIAA Aerospace Sciences Meeting and Exhibit*, 1998; *ASME Wind Energy Symposium*, Reno, NV, USA, January 12-15, 1998.
[37] Hansen, C., AirfoilPrep, NWTC Design Code, Ver. 2.0, [available online] National Renewable Energy Laboratory, Golden, CO, 2005, URL: http://wind.nrel.gov/designcodes/preprocessors/airfoilprep/ [last modified 9 March 2010, accessed 7 December 2012].
[38] Glauert, H., Airplane Propellers, Dover, New York, 1985, pp. 251-268.
[39] Jensen, L. E., "Array Efficiency at Horns Rev and the Effect of Atmospheric Stability," Dong Energy Presentation, 2007.
[40] Shives, M., Crawford, C., "Mesh and Load Distribution Requirements for Actuator Line CFD Simulations", *Wind Energy*, Vol. 15, August 2012.
[41] Rhie, C. M., and Chow W. L., "Numerical Study of the Turbulent Flow Past an Airfoil with Trailing Edge Separation," *AIAA Journal*, Vol. 21, No. 11, 1983, pp. 1525–1532.
[42] Issa, R. I., "Solution of the Implicitly Discretized Fluid Flow Equations by Operator-Splitting," *Journal of Computational Physics*, Vol. 62, 1985, pp. 40–65.
[43] Wesseling, P., "Elements of Computational Fluid Dynamics," Lecture Notes WI4011 TU Delft, 2001.